The Astrophysical Journal, 1000:72 (16pp), 2026 March 20 https://doi.org/10.3847/1538-4357/ae3141
© 2026. The Author(s). Published by the American Astronomical Society.
OPEN ACCESS

A Search for Supermassive Black Hole Binary Candidates in 46 yr Radio Light Curves of 83 Blazars

B. Molina[1], P. Mróz[2], P. V. De la Parra[1], A. C. S. Readhead[3,4], T. Surti[3], M. F. Aller[5], J. D. Scargle[6], R. A. Reeves[1], H. Aller[5], M. C. Begelman[7], R. D. Blandford[8], Y. Ding[9], M. J. Graham[10], F. Harrison[9], T. Hovatta[11,12,13], I. Liodakis[4], M. L. Lister[14], W. Max-Moerbeck[15], V. Pavlidou[4,16], T. J. Pearson[3], V. Ravi[3], A. G. Sullivan[8], A. Synani[4,16], K. Tassis[4,16], S. E. Tremblay[17], and J. A. Zensus[18]
[1] CePIA, Astronomy Department, Universidad de Concepción, Casilla 160-C, Concepción, Chile
[2] Astronomical Observatory, University of Warsaw, Al. Ujazdowskie 4, 00-478 Warszawa, Poland
[3] Owens Valley Radio Observatory, California Institute of Technology, Pasadena, CA 91125, USA; acr@caltech.edu
[4] Institute of Astrophysics, Foundation for Research and Technology-Hellas, GR-71110 Heraklion, Greece
[5] Department of Astronomy, University of Michigan, 323 West Hall, 1085 S. University Avenue, Ann Arbor, MI 48109, USA
[6] Astrobiology and Space Science Division, NASA Ames Research Center (retired), USA
[7] JILA, University of Colorado and National Institute of Standards and Technology, 440 UCB, Boulder, CO 80309-0440, USA
[8] Kavli Institute for Particle Astrophysics and Cosmology, Department of Physics, Stanford University, Stanford, CA 94305, USA
[9] Cahill Center for Astronomy and Astrophysics, California Institute of Technology, Pasadena, CA 91125, USA
[10] Division of Physics, Mathematics, and Astronomy, California Institute of Technology, Pasadena, CA 91125, USA
[11] Finnish Centre for Astronomy with ESO (FINCA), University of Turku, FI-20014 University of Turku, Finland
[12] Aalto University Department of Electronics and Nanoengineering, PL 15500, FI-00076 Espoo, Finland
[13] Aalto University Metsähovi Radio Observatory, Metsähovintie 114, 02540, Kylmälä, Finland
[14] Department of Physics and Astronomy, Purdue University, 525 Northwestern Avenue, West Lafayette, IN 47907, USA
[15] Departamento de Astronomía, Universidad de Chile, Camino El Observatorio 1515, Las Condes, Santiago, Chile
[16] Department of Physics and Institute of Theoretical and Computational Physics, University of Crete, 71003 Heraklion, Greece
[17] National Radio Astronomy Observatory, 1011 Lopez Road, Socorro, NM 87801, USA
[18] Max-Planck-Institut für Radioastronomie, Auf dem Hügel 69, D-53121 Bonn, Germany
Received 2025 September 18; revised 2025 December 12; accepted 2025 December 24; published 2026 March 12

Abstract

The combined University of Michigan Radio Astronomy Observatory and Owens Valley Radio Observatory blazar monitoring programs at 14.5/15 GHz provide uninterrupted light curves of ∼46–50 yr duration for 83 blazars, selected from among the brightest and most rapidly flaring blazars north of declination −20°. In a search for supermassive black hole binary (SMBHB) candidates, we carried out tests for periodic variability using generalized Lomb–Scargle (GLS), weighted wavelet-Z, and sine-wave fitting analyses of this sample. We used simulations to test the effects of the power-law spectrum of the power spectral density (PSD) on our findings, and show that the irregular sampling in the observed light curves has very little effect on the GLS spectra. Apparent periodicities and putative harmonics appear in all 83 of the GLS spectra of the blazars in our sample. We tested the reality of these apparent periodicities and harmonics with simulations, and found that in the overwhelming majority of cases, they must be due to the steep slope of the PSD and the random nature of blazar flares, implying that, in general, apparent periodicities and harmonics in blazar light curves observed in any energy band should be treated with great caution. We find one new SMBHB candidate: PKS 1309+1154, which exhibits a 17.9 yr periodicity. The fraction of SMBHB candidates in our sample is $2.4^{+3.2}_{-0.8}$%.

Unified Astronomy Thesaurus concepts: Relativistic jets (1390)

1. Introduction

Periodicities in the light curves of objects powered by black holes in both stellar mass systems and active galactic nuclei (AGN) are of great scientific interest. They provide a direct probe into the structure of these systems on scales that cannot be probed by imaging with even the highest resolution available to astronomy, i.e., very long baseline interferometry (VLBI), which provides resolution as fine as 20 microarcseconds at submillimeter wavelengths (Event Horizon Telescope Collaboration et al. 2019). Unfortunately, such light curves are much more difficult to interpret than images of resolved structures.

Periodicities in AGN could well be indicative of supermassive black hole binaries (SMBHBs), which are thought to be responsible for a stochastic background of gravitational waves (GWs) with periods of months to years (G. Agazie et al. 2023; EPTA Collaboration 2023; M. T. Miles et al. 2023; N. Agarwal et al. 2026). There are several possible mechanisms other than SMBHBs that could produce periodicities in blazars, such as precession due to warping of the accretion disk (Z. Abraham 2018; S. Britzen et al. 2018), and precession of the relativistic jet due to misalignment of the spin axis of the SMBH and accretion disk (A. Caproni et al. 2004). These may well be viable explanations of potential periodicities in blazars, but we do not consider them further in this paper. In view of their possible importance to the GW stochastic background and the strong theoretical motivation (M. C. Begelman et al. 1980), in this paper we assume that any periodicities found in our studies are due to SMBHBs.

Original content from this work may be used under the terms of the Creative Commons Attribution 4.0 licence. Any further distribution of this work must maintain attribution to the author(s) and the title of the work, journal citation and DOI.

Most blazar light curves are dominated by large flares, but recently, in the Owens Valley Radio Observatory (OVRO) 40 m Telescope monitoring program (J. L. Richards et al. 2011), two blazars have been found in which sinusoidal variations of constant period dominate their light curves much of the time: PKS J0805–0111 and PKS 2131–021 (G.-W. Ren et al. 2021a, 2021b; S. O'Neill et al. 2022, hereafter Paper I; S. Kiehlmann et al. 2025, hereafter Paper II; P. V. de la Parra et al. 2025, hereafter Paper III; A. D. Hincks et al. 2025, hereafter Paper IV). Papers I–IV carried out tests using simulations that take into account the steepness of the power spectral density (PSD) and the probability density function (PDF), and showed that the sinusoidal variations are unlikely to be due to the random nature of blazar flares. PKS J0805–0111 and PKS 2131–021 are, therefore, strong candidates for SMBHBs.

The University of Michigan Radio Astronomical Observatory (UMRAO) 26 m Telescope was dedicated to a blazar monitoring program from 1979–2012.5 (H. D. Aller et al. 1985; M. F. Aller et al. 2014), at the primary frequency of 14.5 GHz. The OVRO 40 m Telescope has been dedicated to an AGN monitoring program of ∼1830 blazars at 15 GHz since 2008. The 83 blazars that are common to these two programs and that were observed continuously from 1979–2025 are the subject of this paper.

In this paper, we report the discovery of strong sinusoidal emission in PKS 1309+1154,[19] with a period of 17.9 yr, based on combined observations from the UMRAO and the OVRO that span the epoch range 1975–2024. Because this window covers only 2.5 periods, PKS 1309 + 1154 is not as strong an SMBHB candidate as PKS J0805–0111 or PKS 2131–021.

Periodicities and possible harmonics in blazar light curves have been discussed in a number of papers (e.g., M. Roy et al. 2000; F. K. Liu et al. 2006; T. An et al. 2013; J.-Y. Wang et al. 2014, 2017; V. S. Bychkova et al. 2015; M. J. Graham et al. 2015; G. Bhatta 2017; A. Tripathi et al. 2021; F.-T. Dong et al. 2022; S. O'Neill et al. 2022; A. Banerjee et al. 2023; X.-P. Li et al. 2023; A. Sharma et al. 2023; S. Abdollahi et al. 2024; L. Mao & X. Zhang 2024; P. V. de la Parra et al. 2025; A. D. Hincks et al. 2025; S. Kiehlmann et al. 2025; G. Liao et al. 2025; A. C. S. Readhead et al. 2026).

We carried out tests for periodic variability in the 83 blazars in the combined UMRAO+OVRO sample using generalized Lomb–Scargle (GLS) periodogram (N. R. Lomb 1976; J. D. Scargle 1982; M. Zechmeister & M. Kürster 2009), weighted wavelet-Z (WWZ; J. R. Ragazzini & L. A. Zadeh 1952; G. Foster 1996), and sine-wave fitting (SWF) analyses. SWF is closely related to GLS, as described in the Appendix. Using all three methods, our tests found *apparent* periodicities in the light curves of *all* 83 blazars in our sample. Simulated light curves matching the PSD of the observed light curves revealed *apparent* harmonics in over 99.9% of the 24,900 cases we tested. Needless to say, these were all false harmonics caused by the steep slope of the PSD.

Thus, in this paper, we show that, in the overwhelming majority of cases, the periodicities and apparent harmonics revealed in blazar light curves through analysis of their variability spectra are likely due to the random nature of blazar flares caused by the steep PSD spectrum. The observing cadence does not matter provided the objects are well sampled on the timescale of the periodicity.

This paper is structured as follows: in Section 2 we discuss the radio observations from the UMRAO and the OVRO; in Section 3 we discuss the search for periodicities in the combined UMRAO+OVRO sample; in Section 4 we discuss other observations of PKS J1309+1154; in Section 5 we carry out an analysis of the harmonics in the blazars in the UMRAO +OVRO sample; in Section 6 we discuss the incidence of SMBHBs among blazars; and in Section 7 we present our conclusions.

2. Radio Observations

The UMRAO blazar monitoring program operated at frequencies 4.8 GHz, 8 GHz, and 14.5 GHz and included measurements of both total flux density and polarization. Only the total flux-density measurements at 14.5 GHz, the primary frequency throughout most of the UMRAO program, are included here. These observations were made using a system of dual, rotating, linearly polarized feed horns symmetrically placed about the parabola's prime focus, which fed a broadband, uncooled high electron mobility transistor amplifier with a bandwidth of 1.68 GHz. An on–on observing technique that alternated beams on the source was employed. Each daily measurement is the average of a series of these individual on–on measurements taken over an interval of 30–40 minutes. The standard deviation associated with each daily flux-density observation was computed from the system noise temperature and the number of individual on–on measurements made on the particular day. The standard error estimates include the effects of measurement noise, the errors introduced by uncertainties in the pointing corrections applied to the observations, and the uncertainties in determining the antenna gain as a function of time; these include both random and systematic contributions. The adopted flux-density scale is based on J. W. M. Baars et al. (1977) and uses Cassiopeia A (3C 461) as the primary flux-density standard. A secondary calibrator, taken from a grid of nearby sources, was observed every 1.5–3 hr to verify the stability of the gain and the accuracy of the pointing. At 14.5 GHz, typically 24 program sources were observed daily, and the highest priority in selecting which sources to include in each observing run (generally 48 hr in duration) was given to measurements of sources exceeding 400 mJy in total flux density in order to provide an adequate signal-to-noise ratio in the polarization measurement. The observing cadence for an individual AGN was determined based on the variability state (flaring or quiescent) at the time of the observation and typically ranged from once a week to once a month for the well-observed AGN included in the sample presented here. As a result, the time windows used in the analysis presented here vary from source to source. The shortest is 18 yr, and the median value for the sample is 32 yr. Observations were made around-the-clock under automatic telescope control, with occasional data gaps due to poor weather, annual source proximity to the Sun, and equipment failures.

The OVRO monitoring program operated on a cadence of once or twice a week. Occasional gaps exist in the data due to weather conditions or hardware problems. The telescope is equipped with a cryogenic receiver. At the start of the monitoring program, this was a Dicke-switched system with bandpass from 13.5–16.5 GHz and center frequency 15.0 GHz.

[19] PKS J1309+1154 is a BL Lac object that has no reliable redshift value (see Section 4.5).

Table 1
Combined UMRAO+OVRO Sample of 83 Blazars

J2000 Name	B1950/C. Name	R.A. (deg)	Decl. (deg)	z	J2000 Name	B1950/C. Name	R.A. (deg)	Decl. (deg)	z
J0010+1058	IIIZW2	2.629	10.975	0.089	J1217+3007	1215+303	184.467	30.117	0.130
J0019+7327	0016+731	4.941	73.458	1.781	J1221+2813	1219+285	185.382	28.233	0.102
J0050-0929	0048-097	12.672	−9.485	0.635	J1224+2122	1222+216	186.227	21.380	0.433
J0102+5824	0059+581	15.691	58.403	0.644	J1229+0203	3C273	187.278	2.052	0.158
J0108+0135	0106+013	17.162	1.583	2.109	J1256-0547	3C279	194.047	−5.789	0.536
J0111+3906	0108+388	17.905	39.108	0.668	J1305-1033	1302-102	196.388	−10.555	0.278
J0112+2244	0109+224	18.024	22.744	0.265	J1309+1154	1307+121	197.391	11.907	*U*
J0136+4751	0133+476	24.244	47.858	0.859	J1310+3220	1308+326	197.619	32.345	0.995
J0204+1514	0202+149	31.210	15.236	0.405	J1337-1257	1334-127	204.416	−12.957	0.539
J0217+7349	0212+735	34.378	73.826	2.346	J1415+1320	1413+135	213.995	13.340	0.247
J0217+0144	0215+015	34.454	1.747	1.715	J1419+5423	1418+546	214.944	54.387	0.152
J0228+6721	0224+671	37.209	67.351	0.523	J1512-0905	1510-089	228.211	−9.100	0.360
J0237+2848	0234+285	39.468	28.802	1.206	J1540+1447	1538+149	235.206	14.796	0.605
J0238+1636	0235+164	39.662	16.616	0.940	J1555+1111	PG 1553+113	238.929	11.190	0.433
J0259+0747	0256+075	44.863	7.794	0.893	J1613+3412	1611+343	243.421	34.213	1.399
J0303+4716	0300+471	45.897	47.271	*U*	J1635+3808	1633+38	248.815	38.134	1.815
J0309+1029	0306+102	47.265	10.488	0.862	J1642+6856	1642+690	250.533	68.944	0.751
J0319+4130	3C84	49.951	41.512	0.018	J1642+3948	3C345	250.745	39.810	0.593
J0336+3218	0333+321	54.125	32.308	1.259	J1653+3945	Mrk 501	253.468	39.760	0.034
J0339-0146	CTA26	54.879	−1.776	0.847	J1719+1745	1717+178	259.804	17.752	0.137
J0418+3801	0415+379	64.589	38.027	0.049	J1733-1304	NRAO 530	263.261	−13.080	0.902
J0423-0120	0420-014	65.816	−1.343	0.913	J1740+5211	1739+522	265.154	52.195	1.379
J0424+0036	0422+004	66.195	0.602	0.268	J1743-0350	1741-038	265.995	−3.834	1.054
J0433+0521	3C120	68.296	5.354	0.033	J1748+7005	1749+701	267.137	70.097	0.770
J0501-0159	0458-020	75.303	−1.987	2.286	J1751+0939	1749+096	267.887	9.650	0.320
J0530+1331	0528+134	82.735	13.532	2.070	J1800+7828	1803+784	270.190	78.468	0.680
J0607-0834	0605-085	91.999	−8.581	0.872	J1806+6949	3C371	271.711	69.824	0.051
J0609-1542	0607-157	92.421	−15.711	0.324	J1824+5651	1823+568	276.029	56.850	0.663
J0721+7120	0716+714	110.473	71.343	*U*	J1927+7358	1928+738	291.952	73.967	0.302
J0730-1141	0727-115	112.580	−11.687	1.591	J2005+7752	2007+777	301.379	77.879	0.342
J0738+1742	0735+178	114.531	17.705	*U*	J2007+4029	2005+403	301.937	40.497	1.736
J0739+0137	0736+017	114.825	1.618	0.189	J2022+6136	2021+614	305.528	61.616	0.227
J0757+0956	0754+100	119.278	9.943	0.266	J2123+0535	2121+053	320.935	5.589	1.941
J0808+4950	0804+499	122.165	49.843	1.435	J2134-0153	PKS 2131-021	323.543	−1.888	1.283
J0818+4222	0814+425	124.567	42.379	*U*	J2158-1501	2155-152	329.526	−15.019	0.672
J0831+0429	0829+046	127.954	4.494	0.175	J2225-0457	3C446	336.447	−4.950	1.404
J0854+2006	OJ287	133.704	20.108	0.306	J2232+1143	CTA102	338.152	11.731	1.037
J0958+6533	0954+658	149.697	65.565	0.367	J2236+2828	2234+282	339.094	28.483	0.795
J1058+0133	1055+018	164.623	1.566	0.891	J2253+1608	3C454.3	343.491	16.148	0.859
J1104+3812	1101+384	166.114	38.209	0.030	J2257+0743	2254+074	344.322	7.720	0.190
J1150+2417	1147+245	177.580	24.298	0.209	J2348-1631	2345-167	357.011	−16.520	0.576
J1159+2914	1156+295	179.883	29.245	0.725	…	…	…	…	…

Note. "*U*" indicates unknown redshift. Redshifts are from the MOJAVE program, except for PG 1553+113, for which we adopt $z = 0.433$ reported by S. D. Johnson et al. (2019) and J. Dorigo Jones et al. (2022).

In 2014, this was changed to a correlation receiver with bandpass from 13.2–17.8 GHz and center frequency 15.5 GHz. The receiver has dual-beam switching to remove atmospheric contributions and background emission, as described by A. C. S. Readhead et al. (1989). At this radio frequency, the observations are confusion-limited, due to the double-switching technique, which combines three separate fields, and the resulting flux-density uncertainty is ∼3–4 mJy. The data reduction and calibration processes used to produce the light curves are described in J. L. Richards et al. (2011).

3. SMBHB Candidates in the Sample of 83 Blazars

The 83 blazars in the combined UMRAO+OVRO sample are listed in Table 1. In testing for periodicities in the light curves of each of these objects, we used GLS periodograms and weighted WWZ transforms, to identify potential SMBHB candidates showing periodicities. In addition, we have developed the SWF approach, described in the Appendix, to search for potential SMBHB candidates revealed through sinusoidal variations in the light curves. We used all three of these methods to search for periodicities in each source in the UMRAO, the OVRO, and the UMRAO+OVRO light curves, separately.

It is important to point out a fundamental distinction that we are making in this paper: we are nowhere claiming that any object in our sample is an SMBHB per se, we are only talking of SMBHB *candidates*.

The results from all three methods are consistent: only one source, PKS J1309+1154, is a potential SMBHB candidate. Its light curve is shown in Figure 1(a), where the black curve shows the least-squares fitted sine wave combined with a

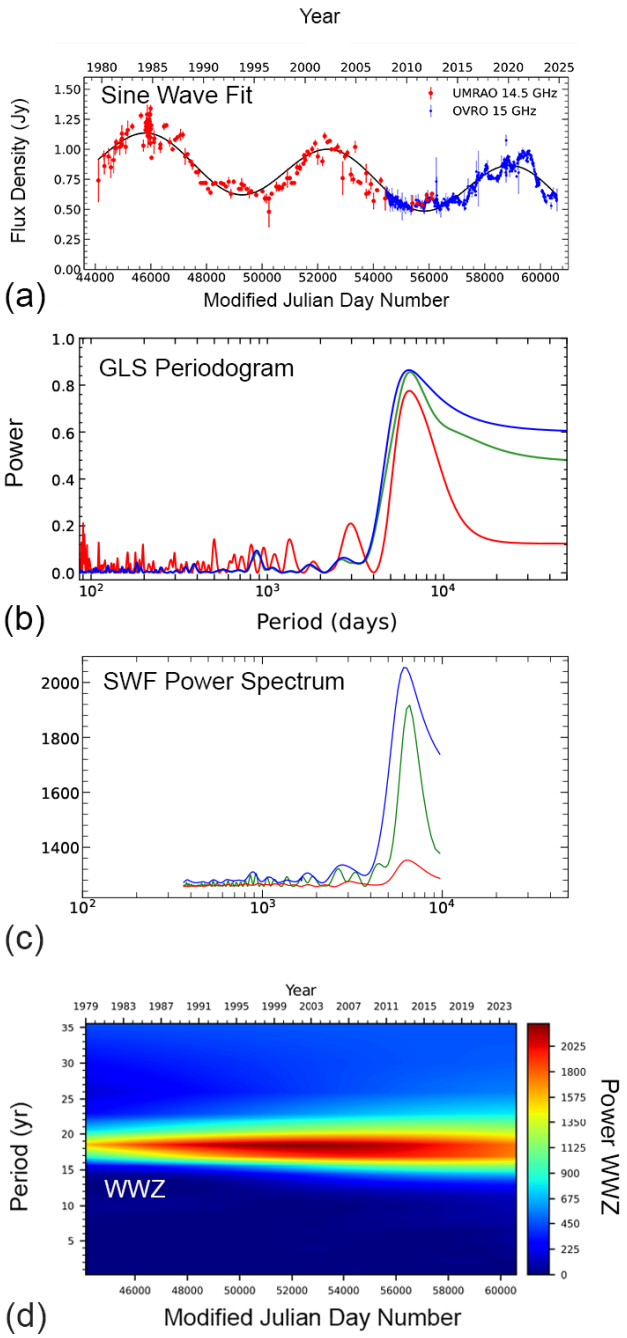

Figure 1. PKS J1309+1154: Panel (a): the combined UMRAO and OVRO light curve. Red and blue symbols denote the UMRAO and OVRO data, respectively. The fitted black sine wave includes a linear downward trend and has period of 6551 days. Panel (b): the GLS periodogram: red, blue, and green curves are the UMRAO, OVRO, and combined UMRAO+OVRO spectra, respectively. Panel (c): the SWF power spectrum. Panel (d): the WWZ wavelet analysis showing only one prominent feature over 46 yr.

linear trend of -0.00755 Jy yr^{-1} to the combined dataset. The period is $P = 6551 \pm 26$ days, determined as described in the Appendix. The GLS analysis of the 83 blazars in our sample shows that PKS J1309+1154 (Figure 1(b)) is the only case in which the strongest GLS peak occurs at the same period in the GLS spectrum in the UMRAO, OVRO, and UMRAO+OVRO light curves. Likewise, the SWF analysis (Figure 1(c) and Table 4 in the Appendix) shows a coherent signal from PKS J1309+1154 in all three light curves . The periods determined by the SWF method for the UMRAO, OVRO, and UMRAO +OVRO light curves are given in the Appendix, where we tabulate them separately. The WWZ spectrum (Figure 1(d)) clearly picks out a single period that dominates over the entire UMRAO+OVRO light curve. None of the other 82 blazars showed a coherent peak over the duration of the observations in the WWZ spectrum.

The results of our SWF analysis shown in Table 4 of the Appendix provide a direct quantitative test of the periodicities in the 83 blazars in our sample. Some of these show the same period in the UMRAO and OVRO data, within the errors, but have periods >30 yr, and large uncertainties. These periodicities are clearly not to be trusted both because of their large uncertainties and because spurious periodicities approaching the length of the observations are very common in blazar light curves. Apart from those cases, *only* PKS J1309+1154 has the same period within the errors (to 1.5σ), with high fractional amplitude in the UMRAO and OVRO light curves and, hence, shows strong coherent sinusoidal variations throughout the 46 yr observing period. Thus, for the purposes of identifying potential SMBHB candidates, we consider *only* PKS J1309 +1154 as an SMBHB candidate, possibly showing the same characteristics as those found in PKS J0805–0111 and PKS 2131–021, discussed in Papers I–IV.

In Papers I and III, we described a method for simulating the light curve of any AGN of particular interest, based on the observed light curve, in which both the PSD and the PDF of the flux-density variations are matched. The simulated light curve is for a Gaussian process with a power-law power spectrum with the same index as observed. This makes it possible to generate large numbers of matching simulated light curves and, hence, to make a reliable estimate of the significance of any feature in the observed light curve compared to random fluctuations taking into account the steepness of the PSD and also taking into account the PDF.

It is important to note that in our estimates of significance, we take into account the "look elsewhere" effect (Paper I). In other words, since we have no a priori reason for picking a particular period, we take into account all of the periods in the all of the simulations of a particular blazar, and not just the observed period. We call the corresponding significance the *global* significance.

In testing for real periodicities, we set a threshold for the global significance at a p-value $= 1.35 \times 10^{-3}$ (i.e., 3σ), and we regard only objects that pass this threshold as *strong* SMBHB candidates. PKS J1309+1154 is not a strong SMBHB candidate by this measure, since it has a global p-value $= 1.06 \times 10^{-2}$ (i.e., 2.3σ). In addition, given that we see only 2.5 cycles in PKS J1309+1154, we do not at this point regard it as a strong SMBHB candidate.

3.1. A Hint of a Harmonic in PKS J1309+1154

The compelling detection of a harmonic in a blazar light curve would be an important development, since it would confirm that the fundamental is not simply a product of the steep PSD spectrum. Harmonics are expected on the kinetic-orbital model of Paper II, but, as discussed in that paper, these are significantly smaller than those we will be considering here.

The fitted sine wave in Figure 1(a) has period $P = 17.9$ yr and amplitude 0.22 Jy. The residual light curve of PKS J1309 +1154 after subtraction of the sine wave plus linear trend,

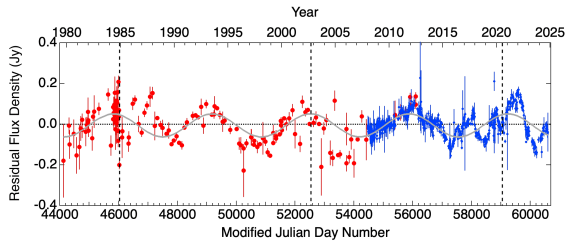

Figure 2. Residual light curve of PKS J1309+1154. The light-gray curve is the least-squares sine-wave fit to the residual light curve. The vertical dashed lines indicate the times of the maxima in the sinusoidal curve in Figure 1(a).

shown by the black curve in Figure 1(a), is shown in Figure 2. This reduced the rms scatter in the light curve by a factor of 2.9, from 0.178–0.062 Jy.

There is a hint of a periodicity in the residual light curve shown in Figure 2, and the least-squares fitted sine wave to this residual light curve has a period of 9.2 yr, which differs by only 3% from the first harmonic of the 17.9 yr period at 8.95 yr. Note that this "harmonic" is the second strongest peak in the GLS periodogram shown in Figure 1(b). Subtraction of this subdominant sinusoidal component reduces the rms scatter in the residual light curve by a further 24%, bringing the rms down by a factor 3.6 relative to that in the original light curve of Figure 1(a).

The amplitude of this first possible harmonic is (26% ± 2%) of the amplitude of the fundamental. In the case of PKS J2131, there is a marginal detection of a first harmonic of amplitude (2% ± 1%) of the fundamental (Paper II).

Thus, PKS J1309+1154 presents a case in which there may be a harmonic in the light curve detectable by successive subtractions of least-squares sine-wave fits. This harmonic is very nearly in phase with the fundamental, the peaks of which are marked by the vertical dashed lines in Figure 2.

We caution, however, that at this point, the evidence for a harmonic is not strong because the sinusoidal variation with a period of 17.9 yr that we have subtracted from the original light curve introduces a periodicity into the light curve such that a fortuitous occurrence of random variations could then mimic a harmonic. At this point, therefore, we regard this as a hint of a harmonic that should be borne in mind, together with the phase relationship, when thinking of physical models for this source.

The confirmation of the harmonic would strengthen the case for PKS J1309+1154 being an SMBHB candidate, which has the advantage that it might possibly be confirmed in 9 yr rather than the 18 yr needed to confirm the reality of the fundamental.

Note that the approach we have adopted above, namely, of selecting the most dominant sinusoidal component by least-squares fitting, subtracting it from the light curve, and then selecting the next-most dominant component, and fitting it by least-squares and subtracting it, is deliberate. We believe this to be preferable to fitting two components simultaneously because it is important to confirm by visual inspection that, at each stage, there is clear evidence of another periodicity in the residual light curve. This approach of successively subtracting a feature and then examining the residual for the next-most-prominent feature is the same as that used with great success in image restoration using the CLEAN method. (e.g., T. J. Pearson & A. C. S. Readhead 1984) In that method, successive components are subtracted from a "dirty" image only when there is clear evidence for that component in the residual map.

4. Other Observations of PKS J1309+1154

In this section we describe other observations of PKS J1309+1154 and show that there are several similarities with PKS 2131-021, which, while not definitive, are certainly suggestive of a common cause of the periodicities seen in these two objects.

4.1. VLBA Observations of PKS J1309+1154

The Monitoring of Jets in Active Galactic Nuclei with VLBA Experiments (MOJAVE) program (M. L. Lister et al. 2021) monitors bright radio-loud AGN using high-resolution Very Long Baseline Array (VLBA) observations at 15 GHz. Fortunately, PKS J1309+1154 has been observed 13 times on the MOJAVE program. We undertook an analysis of the MOJAVE results on PKS J1309+1154 to determine whether the observed long-term periodic modulation originates in the core or the jet.

The total flux densities of the core and the jet, at a number of epochs, are provided by MOJAVE as part of their long-term monitoring program. The corresponding published model-fitted components are available on the VizieR catalog service (M. L. Lister et al. 2023), which were taken from the supplementary material (J/ApJ/923/30/table4) of M. L. Lister et al. (2021). The component models were derived by Lister and collaborators using Gaussian model fits to the VLBA visibility curves with the DIFMAP software (M. C. Shepherd et al. 1994; M. C. Shepherd 1997). The entry for each component includes the peak flux density, the radial separation from the core, the position angle, the FWHM size of the component's major axis, and its axial ratio. We retrieved the component data for multiple epochs. There is one epoch from 1999 and a series of epochs spanning 2011–2019.

4.2. The Stationary Component

Of the 83 blazars in the combined UMRAO+OVRO sample, in 40% of them, the components within a beamwidth of the core are stationary. The positions of component #5 relative to the core for the MOJAVE observations of PKS J1309+1154 and PKS 2131–021 are shown in Figure 3 and listed in Table 2.

We see that the position of component #5 relative to the core can be measured with high precision, and that it is unchanging in both blazars. In VLBI, it is possible to measure the distance between components with an uncertainty equal to the beamwidth divided by the signal-to-noise ratio, when the signal-to-noise ratio is high as it is here, by model fitting in the (u, v) plane.

In Figure 4 we show the flux densities of the key components together with the UMRAO+OVRO light curve showing the total flux densities over the relevant epochs.

Since the sinusoidal variations in total flux density dominate the light curve, it is easy to determine which components in the VLBA decompositions contribute to this variation. While we do not have VLBA maps throughout the whole period monitored, we do have maps over two cycles of the sinusoid in PKS 2131–021 and over half a cycle of the sinusoid in the case of PKS J1309+1154. As can be seen in Figure 4, the combined flux densities of the core plus component #5

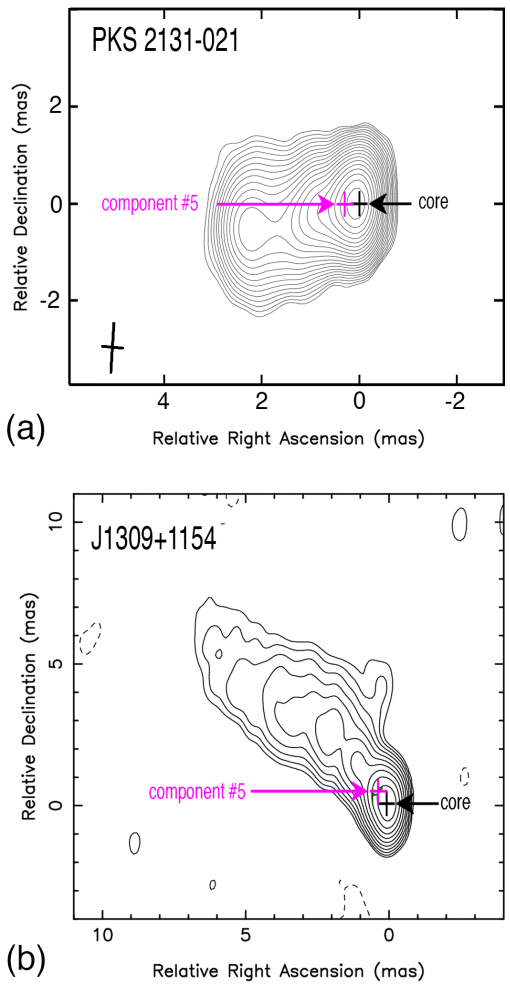

Figure 3. VLBA 15 GHz MOJAVE maps of (a) PKS 2131–021 and (b) PKS J1309+1154, showing the close juxtaposition of the stationary component #5 and the core. In both cases, the sinusoidal variations originate not only in the core, but also in component #5.

dominate the flux-density variations. It is clear, therefore, that the sinusoidal variations in total flux density seen in these two objects originate in these two components, i.e., the cores and components #5.

4.2.1. Possible Explanation for the Stationary Components

Stationary components in the jets of blazars have been much discussed in the literature (e.g., M. H. Cohen et al. 2014, 2015; T. G. Arshakian et al. 2020, 2024, 2025; Z. R. Weaver et al. 2022), and are usually ascribed to standing shocks in the jet. Here we offer an alternative explanation.

In the context of a binary black hole interpretation, sinusoidal variation of blazar flux density is associated with orbital motion of the jet source with period P. The simplest models suppose that the direction of the jet launch velocity is modulated by the orbital velocity. The variation is determined more by the changing direction than the changing speed. If the pattern speed of the modulation is ultrarelativistic, the emission seen at a given observer time may originate from radii $\gg 10\,cP$ due to relativistic effects. Having coherent variation in emission regions separated by $\sim$100 pc seems highly unlikely (A. D. Hincks et al. 2025; S. Kiehlmann et al. 2025; A. G. Sullivan et al. 2026).

An alternative model (see Figure 5) posits that the jet direction is determined by the orbital motion of the confining medium, most reasonably, though not necessarily, a non-relativistic MHD wind. The jet keeps an ultrarelativistic speed within a channel carved out by the wind, but the pattern speed of the variation becomes much slower due to the jet-wind boundary interaction (A. G. Sullivan et al. 2026). In this case, the variable emission comes from a range of radii separated by $\lesssim 10\,cP$ (A. G. Sullivan et al. 2026). If this model is relevant, then it is tempting to identify the "stationary" jet component seen in PKS J1309+1154 and PKS 2131−021, and perhaps other sources, with the outer radius of the confining wind before the interaction is dominated by the surrounding interstellar medium, which, presumably does not share the orbital motion. It is natural to associate this with a Bondi or recollimation radius (e.g., R. Blandford et al. 2019), which could exhibit flux modulation without proper motion. The actual radius of this component is likely $\gtrsim 10\,cP$. Future magnetohydrodynamic simulations of orbiting jets, disks, and winds should be instructive.

4.3. Polarization of PKS J1309+1154 at 14.5 GHz

The total linear polarization of PKS J1309+1154 was monitored at the UMRAO at 14.5 GHz for the duration of the light curve, and is shown in Figure 6. The mean electric vector position angle (EVPA), which is dominated by the core and inner jet, is 39.1° ± 1.7°, which may be compared with the position angle of component #5 relative to the core given in Table. 2, of 37.3° ± 0.7°. Thus, the difference between the position angle of the inner jet and the EVPA is 1.8° ± 1.9°. This shows that the magnetic field is perpendicular to the jet axis, i.e., it is a helical magnetic field, as is also the case in PKS 2131-021. The stacked MOJAVE polarization map of PKS J1309+1154 is shown in Figure 7.

4.4. ALMA Observations of PKS J1309+1154

We downloaded Atacama Large Millimeter/submillimeter Array (ALMA) data from the ALMA calibrator website. ALMA has observed PKS J1309+1154 a number of times in Band 3 (at 91.5 and 104 GHz). Since the data are few and almost all of the observations were made at both frequencies, we make no distinction, but refer to them as "Band 3."

In Figure 8 we show the ALMA Band 3 and OVRO light curves of PKS J1309+1154. As discussed in detail in Paper II, when comparing sinusoidal variations at different frequencies, it is important to fit the sine wave over the window of the observations. This is because, as discussed in detail in Paper I, random correlated variations in the nonsinusoidally varying components cause apparent variations in the period of the sinusoid of up to 10%. For this reason, we do not use the period of the whole UMRAO+OVRO light curve in this comparison with the ALMA data, but only that of the OVRO data.

We have carried out a least-squares fit to the OVRO light curve of Figure 8, and we find a period of 6201 days (16.5 yr), i.e., 8% shorter than the period fitted over the full 46 yr. We then held this period fixed and fitted the sine wave to the ALMA data shown in Figure 8. The two sine waves are offset in phase by -300^{+260}_{-200} days, with the higher-frequency observations leading the lower, although the uncertainties are large. This same phenomenon has been seen in both PKS 2131

Table 2
Position of Component #5 Relative to the Core in the Jets of PKS J1309+1154 and PKS 2131–021

PKS J1309+1154 Date	PKS J1309+1154 Separation (mas)	PKS J1309+1154 Position Angle	PKS 2131–021 Date	PKS 2131–021 Separation (mas)	PKS 2131–021 Position Angle
2011 December 29	0.48	35.8°	2001 March 15	0.29	85.7°
2012 June 25	0.46	36.5°	2002 May 8	0.36	91.1°
2012 November 2	0.47	37°	2002 August 7	0.36	93.2°
2013 January 21	0.48	38.5°	2003 May 9	0.29	93.4°
2013 June 2	0.44	40.7°	2003 August 28	0.32	96.0°
2014 February 14	0.49	41.1°	2004 August 9	0.33	91.8°
2015 January 18	0.51	39°	2004 September 2	0.33	94.9°
2015 September 6	0.49	38.8°	2004 December 2	0.30	87.0°
2016 July 16	0.46	34.9	2005 November 17	0.33	93.3°
2016 November 12	0.47	33.8	2006 August 9	0.34	93.0
2019 April 15	0.47	35.6°	2007 February 5	0.30	93.4°
2019 August 4	0.49	35.9°	2007 June 10	0.28	88.4°
…	…	…	2007 August 16	0.27	88.3°
…	…	…	2008 September 12	0.31	91.6°
…	…	…	2009 February 25	0.31	90.1°
…	…	…	2010 March 10	0.31	92.9°
…	…	…	2010 June 27	0.30	94.1°
…	…	…	2011 April 11	0.30	91.7°
…	…	…	2012 May 24	0.30	91.6°
Mean	0.476	37.3	Mean	0.312	91.7°
Standard deviation	±0.018	±2.3	Standard deviation	±0.024	±2.7°
Std error in mean	±0.006	±0.7	Std error in mean	±0.006	±0.6°

Note. The standard deviations indicate the rms scatter in the measurements, and show that these values repeat with high precision from epoch to epoch, so that the standard error in the mean is very small, and consequently there is no doubt that component #5 is stationary relative to the core to within these uncertainties in both PKS J1309+1154 and PKS 2131–021. These values are all from the MOJAVE program.

−021 and PKS J0805−0111. In the case of PKS 2131−021, the ALMA Band 3 variations lead the OVRO 15 GHz variations by 0.075 ± 0.005 of a period (Paper II). In the case of PKS J0805−0111, the ACT 95 GHz variations lead the OVRO observations by 0.0.131 ± 0.006 of a period (Paper IV). In this case, we see that the ALMA Band 3 sinusoidal variation leads that of OVRO at 15 GHz by $0.05^{+0.4}_{-0.3}$ of a period.

The similarity, with respect to the small phase shift, between PKS J1309+1154 and the two strong SMBHB candidates, PKS 2131−021 and PKS J0805−0111, provides more evidence suggesting that PKS J1309+1154 is a good, albeit not a strong, SMBHB candidate.

4.5. Optical and Infrared Observations of PKS J1309+1154

Before discussing the optical and infrared properties of PKS J1309+1154, we first consider those of the SMBHB candidate PKS 2131–021. PKS 2131–021 has recently been shown to have coherent sinusoidal variations from radio to the optical wavelengths, exhibiting a strong correlation between phase and the observed frequency. According to the kinetic-orbital model (Papers I and II; A. G. Sullivan et al. 2026), this phase shift is due to the fact that the higher-frequency emission originates farther down the blazar jet axis closer to the binary.

We have therefore assembled optical and infrared observations of PKS J1309+1154, to determine whether the radio sinusoidal variations can also be seen in other wave bands.

PKS J1309+1154 has been monitored at optical wavelengths spanning about 19.25 yr (MJD 53500–MJD 60500) by the Catalina Real Time Transient Survey (CRTS; A. J. Drake et al. 2009) and later the Zwicky Transient Facility (ZTF; E. C. Bellm et al. 2019) with a gap in coverage between the two surveys of ∼800 days. In Figure 9, we show the optical light curves, noting that CRTS has no standard filter. We discard a single erroneous measurement that is 2 mag brighter than the rest of the data. We appended multiepoch ALLWISE and NEOWISE W1 and W2-band photometry (A. Mainzer et al. 2011; E. L. Wright et al. 2019), shifted up by 3 mag for easier comparison to the optical photometry.

While they show some modulation, the optical light curves do not show a clear modulation with the period detected by the UMRAO and OVRO light curves. Visually, there appears to be a maximum around 2007–2008 in the CRTS light curve, and the ZTF data might be rising toward a maximum either around 2022 or after 2024 despite when accounting for an overall decreasing trend in the combined optical light curves.

If we combine the CRTS light curve (calibrated to ZTF *r*) with the ZTF *r*-band light curve and convert to fluxes, a GLS analysis reveals a signal at 24 yr periodicity with a GLS power of $\mathcal{P} = 0.50$.[20] Alternatively, given that the *r*-band data appear to exhibit a slow decreasing trend, de-trending the *r*-band light curves using a linear fit results in two signals at periods of ∼7.5 yr with power $\mathcal{P} = 0.42$ and ∼17.1 yr with power $\mathcal{P} = 0.37$. Finally, combining all optical data, a multiband LS analysis using ASTROPY's LOMBSCARGLEMULTIBAND (based on J. T. VanderPlas & Ž. Ivezić 2015) reveals a periodicity at 11 yr with a power of $\mathcal{P} = 0.47$. These signals are relatively weak and individually inconsistent with the radio period of 17.9 yr; a coherent sinusoidal variation cannot be

[20] To distinguish the GLS power from the period of the periodicity, *P*, we use the symbol $\mathcal{P}$ to denote the GLS power.

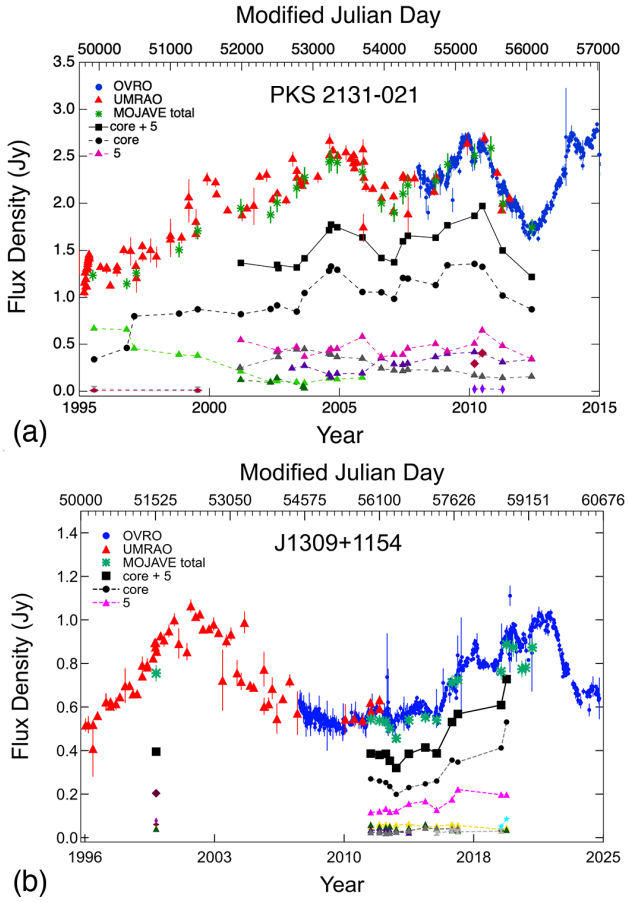

Figure 4. UMRAO+OVRO monitoring and MOJAVE VLBA results on PKS J1309+1154 and PKS 2131–021. (a) PKS 2131–021 adapted from Paper I. (b) PKS J1309+1154 from MOJAVE. In both cases, the combined flux densities of the core component and component #5 follow the total flux density and are clearly the major contributors to the sinusoidal variation. It is just coincidental that in both sources, the stationary component is #5.

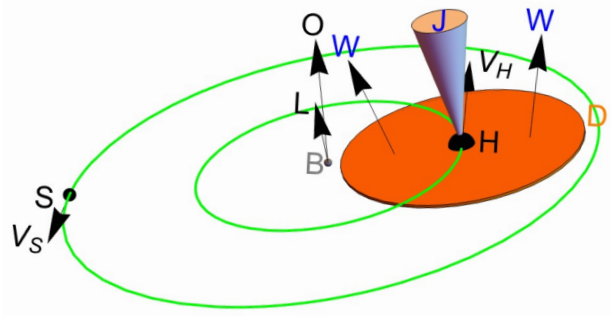

Figure 5. Illustration of the model from A. G. Sullivan et al. (2026). An SMBHB composed of the primary black hole H and a secondary black hole S. Note that H orbits with speed v_H, carries around a disk (D), and launches a jet (J) along the orbital angular momentum direction (L). The disk produces a wind (W) with speed $v_w < c$, which collimates the jet.

concluded with the current optical data. However, these signals do bracket the radio period, and we note that the phase of the CRTS peak at MJD 52473 under a period of 17.9 is ~ -0.3. This is broadly consistent with the NIR and optical phase shifts observed in PKS 2131–021 (being -0.27 and -0.35, respectively). Therefore, the possibility of coherent variation

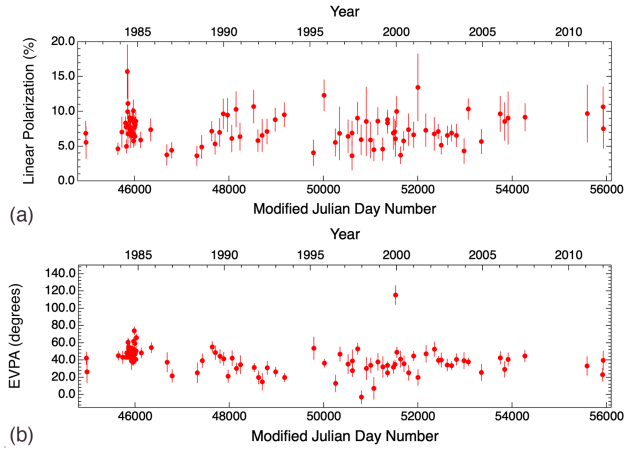

Figure 6. The polarization of PKS J1309+1154 at 14.5 GHz from the UMRAO monitoring survey. Panel (a): the fractional linear polarization. Panel (b): the electric vector position angle (EVPA). The mean EVPA is aligned with the inner jet axis.

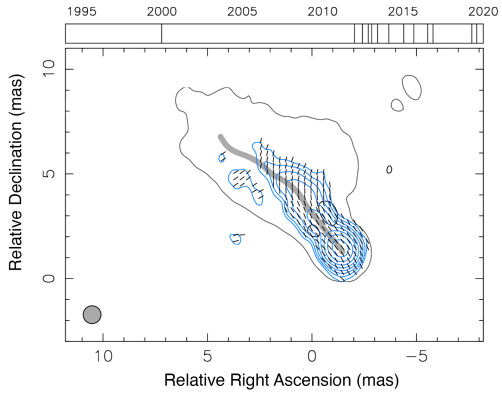

Figure 7. Stacked MOJAVE polarization map of PKS J1309+1154 for the 13 epochs for which it was observed, adapted from A. B. Pushkarev et al. (2023). The vertical bars above the map indicate the epochs of observation. The gray line indicates the ridge line of the jet. The EVPA vectors are indicated by the short black lines.

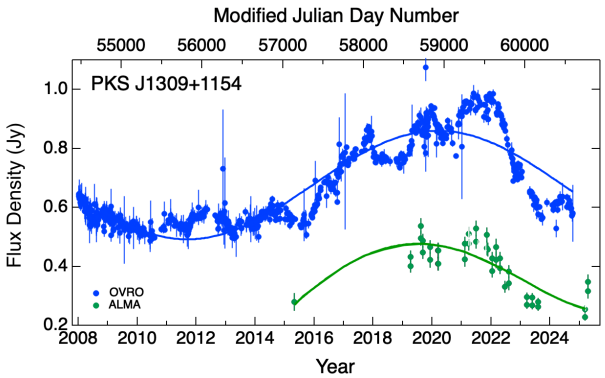

Figure 8. The OVRO (blue) and ALMA (green) light curves of PKS J1309 +1154, together with their least-squares sine wave fits.

in the optical should not be ruled out without observations spanning a longer duration.

We note that two redshifts have been cited for PKS J1309 +1154 in the literature: a photometric redshift of $z = 0.415$ from (G. T. Richards et al. 2009; Sloan Digital Sky Survey, SDSS, DR6) and later a spectroscopic $z = 1.415$ from

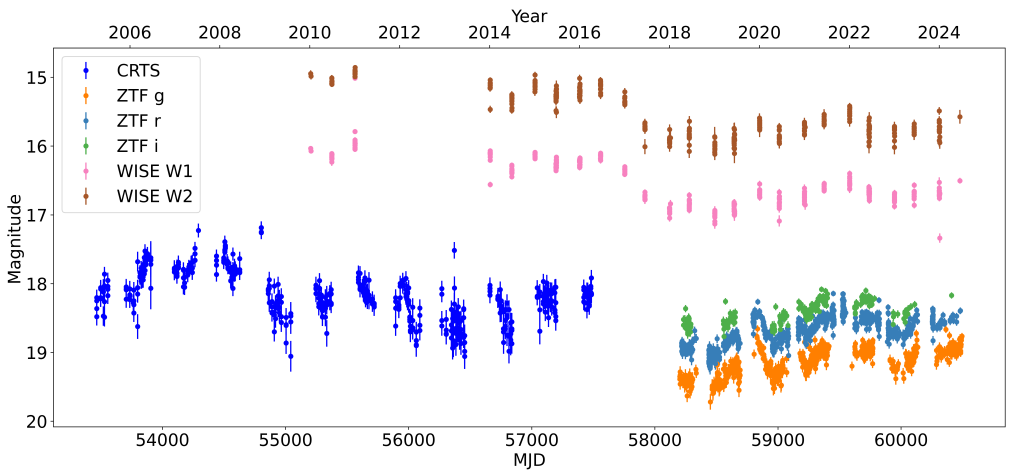

Figure 9. Optical (CRTS and ZTF *gri*-band) and NIR (Wide-field Infrared Survey Explorer, WISE, W1- and W2-band) light curves for PKS J1309+1154. W1 and W2 magnitudes are shifted up by 3 mag for clarity.

(F. D. Albareti et al. 2017; SDSS DR13). However, the SDSS BOSS spectrum reveals an effectively featureless optical spectrum typical of blazars,[21] leading us to conclude that no reliable redshift estimate can be determined. At least two absorption systems are evident in the BOSS spectrum, at redshifts of 0.515 and 0.852, traced primarily by the Mg II $\lambda\lambda$2796, 2803 doublet. Thus, PKS J1309+1154 is at a redshift $z \geqslant 0.852$.

4.6. X-Ray Observations of PKS J1309+1154

PKS J1309+1154 was observed by Swift-XRT during the past decades. We extracted and combined legacy X-ray spectra using the archival data on the UK Swift Science Data Centre (UKSSDC). The final combined spectrum has an effective exposure time of 8486s in the 0.3–10 keV band. The combined spectrum is binned to have at least 1 count bin^{-1} and avoid empty channels (with FTGROUPPHA). The final spectrum has 339 bins.

Models were fitted to the X-ray spectrum using XSPEC (K. A. Arnaud 1996). During the fitting, the modified Cash statistic included Galactic foreground absorption of $1.9 \times 10^{20}\,\mathrm{cm}^{-2}$. We find that the X-ray spectrum can be well fitted with a power law of a photon index of $\Gamma = 1.28 \pm 0.26$ (C-stat/DoF = 227.2/337), significantly harder than other blazars that show strong evidence of sinusoidal variation ($\Gamma \simeq 1.8 - 2.2$ for PKS 2131–021 and PKS 0805–011). At this early stage of uncovering the phenomenology of SMBHB candidates, the significance of this difference is unclear. We estimate the total flux in 0.3–10 keV from the best-fit model to be $7.5 \times 10^{-13}\,\mathrm{erg\,s^{-1}\,cm^{-2}}$ (in the observer's frame). Simulations have predicted that close-separation accreting SMBHBs may have a periodically modulated hard X-ray component whose period is around the binary orbital period (Y. Tang et al. 2018; J. H. Krolik et al. 2019). Future X-ray timing studies with large field-of-view X-ray instruments (e.g., Swift and eRosita) could help unveil the nature of this target.

[21] https://specdash.idies.jhu.edu/?catalog=sdss&specid=6104739071615326208

5. "Harmonics" in Blazar Light Curves

A number of blazars have been reported as showing multiple periodicities, some of which are harmonics, in their radio, optical, or gamma-ray light curves (e.g., M. Roy et al. 2000; F. K. Liu et al. 2006; T. An et al. 2013; J.-Y. Wang et al. 2014; G. Bhatta 2017; A. Tripathi et al. 2021; F.-T. Dong et al. 2022; A. Banerjee et al. 2023; A. Sharma et al. 2023; L. Mao & X. Zhang 2024; G. Liao et al. 2025).

We find that we can have confidence in the spectral peaks identified by these methods only in cases where the GLS spectra are dominated by a single long-lived sinusoidal component, such as is the case, for example, in PKS 2131–021 (Papers I and II), in PKS J0805–0111 (Paper III), and in PKS J1309+1154 (Figure 1). In the last case, only ~2.5 cycles have been observed, so the consistent GLS and WWZ spectra and the good sinusoidal fit shown in Figure 1 could well be a transient characteristic of this source. Among our 83 sources, there are many that, for short durations, exhibit similar features.

Although the standard GLS analysis method can detect multiple peaks indicative of multiple sinusoidal periodicities in blazar light curves, the model behind it is a single sinusoid embedded in white noise (J. D. Scargle 1982; G. L. Bretthorst 2003). Therefore, in principle, the standard GLS model is inappropriate for a light curve with two sinusoidal components. However, in practice, the standard GLS power spectrum reliably detects sinusoidal components if their frequencies are resolved—that is, separated in frequency by more than the width of the spectral window function, and this is what we have used in this paper. At the end of this study, we became aware of the extension of the standard GLS model to the case of "multiharmonic" periodograms (R. V. Baluev 2009; M. Seilmayer et al. 2020), and we have started an investigation of this approach together with a machine learning approach.

Apart from PKS J1309+1154, the variability spectra of the other 82 blazars from 1979–2008 were markedly different from their counterparts between 2008 and 2025. This demonstrates clearly that we are not observing a statistically stationary phenomenon in blazar light curves, even with a time span of 16 yr.

An illuminating example is that of 3C 279, shown in Figure 10. The UMRAO and OVRO light curves shown in

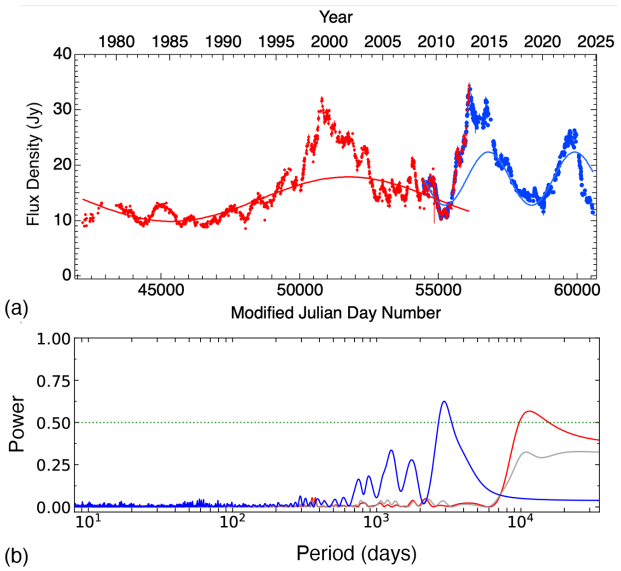

Figure 10. Light curves and GLS spectra of 3C 279. Panel (a): the combined UMRAO 14.5 GHz and OVRO 15 GHz light curves (red points:UMRAO, blue points:OVRO). The fitted sine waves have periods $P = 12,788$ days and $P = 3,118$ days for UMRAO and OVRO, respectively (see Table 4). Panel (b): the GLS spectra of the UMRAO light curve (red), the OVRO light curve (blue), and the combined UMRAO+OVRO light curve (gray). The green dotted line marks the $\mathcal{P} = 50\%$ power level (see the text).

Figure 10(a) look fairly similar, and they overlap for 4 yr (2008–2012). Nevertheless, the GLS spectra shown in Figure 10(b) are qualitatively very different. The OVRO GLS spectrum exhibits a number of peaks with powers between 0.2 and 0.4, whereas the UMRAO spectrum exhibits no peaks having power greater than $\mathcal{P} = 7\%$ apart from that associated with the longest period peak. One might think that this difference arises partly because there might be more power in that peak, but its power is $\mathcal{P} = 66\%$, i.e., not that different to the power in the largest OVRO peak ($\mathcal{P} = 63\%$). Thus, even strong GLS peaks having power $\mathcal{P} > 0.6$ that are a factor $\gtrsim 2$ stronger than the other peaks in the GLS spectrum are not indicative of true periodicities in the blazar. There are, furthermore, many harmonic relationships between the periods of the peaks in both the UMRAO and the OVRO GLS spectra. The striking differences between the GLS spectra for UMRAO and OVRO, which are similar to those seen in many of our sources, show that these periodicities and their harmonics are not stable, reproducible features of these blazars. Note that, in the combined 50 yr UMRAO+OVRO GLS spectrum of 3C 279 shown in Figure 10(b), apart from the two peaks with periods above 10^4 days, the largest peak has a power of only $\mathcal{P} = 5.1\%$, while the others are 4% and lower. This shows that the power is spread across the variability spectrum even in the presence of large fractional flux-density variations. This example shows that even for GLS peaks with power as high as $\mathcal{P} = 60\%$, the main periodicity should be interpreted with caution. Clearly, the much lower powers of the apparent harmonics should be interpreted with still more caution.

5.1. Harmonics in Simulated Light Curves

In this section we present a comparison between the apparent periodicities in the 83 blazars in our sample, as revealed through GLS periodogram analysis, with simulated light curves constructed as described above in Section 3.

We simulate light curves with the same statistical and variation characteristics as the observed light curves, using the methods introduced by J. Timmer & M. Koenig (1995) and D. Emmanoulopoulos et al. (2013) to produce light curves that match both the PSD and the PDF of the observed light curve (Papers I, II, and III).

In order to test the reality of the apparent harmonics we see in our GLS spectra of all 83 blazars in our sample, we generated 300 pure random noise simulations with no coherent sinusoids added, to match the cadence and noise characteristics of each of our 83 blazars.

We constructed 100 simulations for each of the three different power-law PSD slopes: $\beta = -1.5$, $\beta = -1.9$, and $\beta = -2.5$ for each blazar. We then carried out GLS spectral analysis of these 24,900 simulated light curves. The GLS periodogram was evaluated over the frequency range from $f_{\rm low} = 1/(1.8 \times T)$ to $f_{\rm high} = \min(1.1 \times N/(2 \times T), 1/(2 \times \Delta t_{\rm med}))$, where T is the total observing time, N is the total number of measurements, and $\Delta t_{\rm med}$ is the median sampling interval. When selecting the six strongest peaks, we considered only those with periods $P > 100$ days. For this study, we used a high value of $\zeta = 29$ in order to be able to measure the periods of the peaks with high accuracy.

Note that the above values of β span the range of PSD slopes seen in many blazars at optical wavelengths in which the variations may be characterized by a damped random walk with a turnover from $\beta = -2$ to $\beta = 0$ at frequencies that can be below 10^{-3} day^{-1} (B. C. Kelly et al. 2014; M. J. Graham et al. 2017), corresponding to periods of years.

In each of the observed and simulated light curves, we identified the six most powerful GLS peaks. In Figure 11, we show the distribution of the powers of these six peaks from our simulations with $\beta = -1.5$, $\beta = -1.9$, and $\beta = -2.5$, compared to the observed powers in the corresponding peaks. The distribution for the case $\beta = -1.5$ matches the observed distribution most closely, so we adopt that as our fiducial case.

We next searched for independent harmonics in which the period ratios were 4/3, 3/2, 2/1, 3/1, and 4/1, where we counted as harmonics any match within 10% of one of the above ratios or its reciprocal. The results are shown in Table 3. We see that there are, on average, 4.5 ± 0.23 harmonics per observed light curve, and 3.8 ± 0.02 harmonics per simulated light curve. The ratio of the number of harmonics per observed light curve to the number of harmonics per simulated light curve is therefore 1.17 ± 0.06, which hints at a difference that is significant at just below the 3σ level, where we are using $\sqrt{N}$ for our σ estimates. It should be borne in mind that the simulations assume a strict power-law dependence, whereas the actual shapes of the observed PSDs are more complex. Thus, there is some uncertainty that is not included in the uncertainty in the number of simulated harmonics in Table 3. Nevertheless, especially given the hint of a harmonic that we found by hand in the analysis of the light curve of PKS J1309+1154, this slight difference should not be totally ignored.

Our results with the other assumed slopes of the PSD show that power-law slopes of $\beta = -1.9$ and $\beta = -2.5$ return almost identical results to those assuming $\beta = -1.5$. Thus, the occurrence of harmonics is independent of the power-law slope over this range of β.

Our conclusion from the above analysis is that the close agreement between the observed and the simulated number of

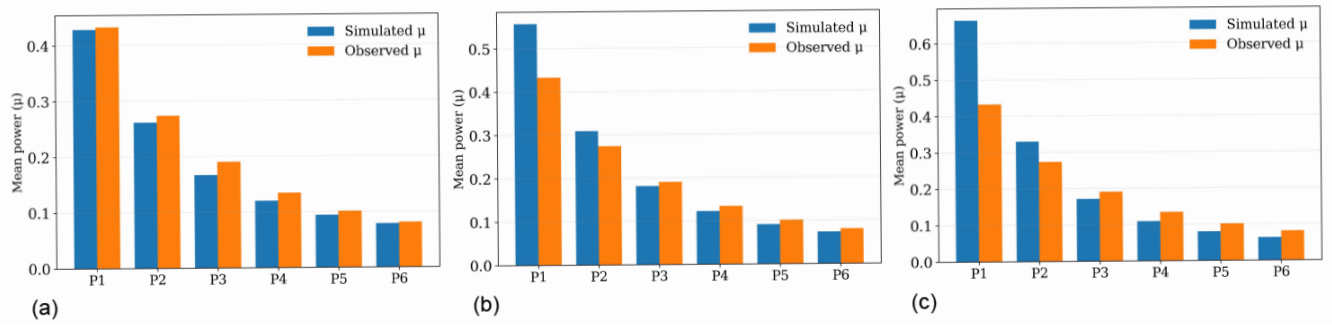

Figure 11. The mean powers of the six most powerful peaks in the GLS spectra of the simulations compared to the observations: (a) for $\beta = -1.5$, (b) for $\beta = -1.9$, and (c) for $\beta = -2.5$.

Table 3
Comparison of the Harmonics in the Observed versus Simulated Light Curves for $\beta = -1.5$

Category	Number of Light Curves	Number of Harmonics	Harmonics per Source	Ratio of Observed to Simulated Harmonics per Source
Observed	83	371 ± 19	4.47 ± 0.23	1.17 ± 0.06
Simulated	8300	31, 720 ± 178	3.82 ± 0.02	...

Note. All uncertainties on N are assumed to be $\sqrt{N}$. Numbers above are for the case $\beta = -1.5$. Almost identical results are obtained for $\beta = -1.9$, and $\beta = -2.5$.

harmonics per source is proof that the steep slope of the PSD produces random flares that are responsible for the vast majority of periodicities and harmonics seen in blazar GLS spectra.

As an illustrative example, we carried out the same least-squares sine subtraction analysis of the light curve of J0019+7327 (see Figure 12) that we used in the case of PKS J1309+1154 described in Section 3. We have chosen J0019+7327 because its GLS spectrum is particularly interesting, since its two strongest peaks have power $\mathcal{P} \approx 0.5$ with periods that differ by a factor 2. We first fitted a simple sine-wave model and obtained a period of 25.2 ± 0.2 yr. We then added a $P/2$ component and fitted both components simultaneously, allowing the period to vary, but maintaining the period ratio of 2. This yielded the period 25.7 ± 0.2 yr. The light curve and corresponding fits are shown in Figure 12(a). It is clear that the data do not strongly support the existence of these two sinusoidal periods. This is borne out by the fact that when the first sinusoid (orange curve in Figure 12(a)) is subtracted, the rms of the residual is reduced only by 30%, and this is only reduced by a further 5% when the two sinusoids (green curve in Figure 12(a)) are subtracted. For comparison, when the fitted sinusoid of PKS 2131–021 (Papers 1 and 2) is subtracted, the rms decreases by a factor 3. In PKS J1309+1154, when the linear trend and fitted sinusoid shown in Figure 1(a) are subtracted, the rms decreases by a factor 2.9, and when the harmonic is subtracted, the rms scatter decreases by a further 24%.

Finally, we tested whether the harmonics could be significantly affected by the cadence of the observations, i.e., the average number of observations per unit time. In Figure 13 we show the result of such a test on a simulated light curve of AO 0235+164. The cadence is clearly not responsible for producing the periodicities and harmonics we are seeing in our blazar light curves.

It is clear, therefore, that in the vast majority of cases, it is the random nature of blazar flares that leads to the multiple peaks in GLS spectra, frequently with apparent harmonic relationships and, therefore, that neither of these is due to the dynamics of the SMBHs and their associated accretion disks.

6. The Incidence of SMBHB Candidates among Blazars

In this section we discuss two aspects of the numbers of SMBHB candidates among blazars. We first compare the numbers of SMBHB candidate in the 16 yr OVRO light curves with those in the 46 yr UMRAO+OVRO light curves, and we then consider the fractions of SMBHB candidates that our results imply.

6.1. The Predicted Number of Strong SMBHB Candidates in the UMRAO+OVRO Light Curves of 83 Blazars

The number of SMBHBs detected in a light-curve monitoring program depends strongly on the duration τ of the observations. One can only detect SMBHBs having periods, P, less than a maximum, $P_{\rm max}$, that is set by τ. We adopt $P_{\rm max} = 0.3\tau$, i.e., SMBHB candidates should be observed for at least 3.5 cycles in order to be classified as strong candidates.

M. C. Begelman et al. (1980) first described the evolutionary stages of an SMBHB as the orbit shrinks. Once the binary becomes sufficiently tightly bound, the orbit is circularized, and gravitational radiation dominates the energy-loss timescale. Thereafter, gravitational radiation shrinks the orbit on a timescale $t_{\rm GR} \propto r^4$, where r is the separation of the black holes in the binary.

Let the number of SMBHBs, N, with separation less than r be $N(<r)$. Clearly $N(<r) \propto r^4$. By Kepler's law $r \propto P^{2/3}$. Thus, for any given combined SMBHB mass, $N(<P) \propto r^4 \propto P^{8/3}$. Therefore, in observations of duration τ_1, versus observations of duration τ_2, the ratio of the numbers of sources in which we might expect to detect strong sinusoidal fluctuations, $N_2/N_1 = [\tau_2/\tau_1]^{(8/3)}$.

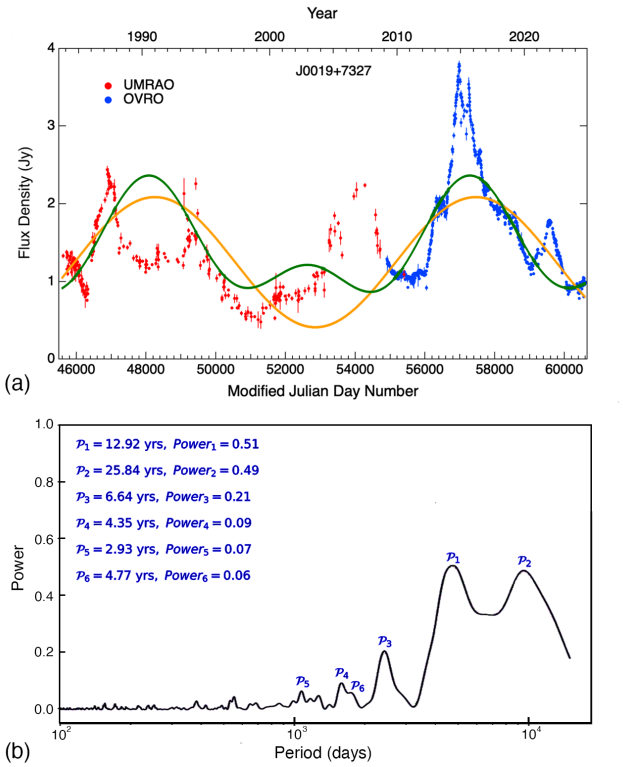

Figure 12. Light curve and GLS spectrum of J0019+7327. Panel (a): the UMRAO+OVRO light curve: red points—UMRAO data, blue points—OVRO data. The orange curve shows the original fit of a sinusoid to the data. The green curve shows the fit when a second sinusoidal component of half the period is added (see the text). Panel (b): GLS spectrum of the UMRAO +OVRO light curve shown in panel (a). The two brightest peaks have almost equal powers of $\mathcal{P}$=∼50%, and their periods differ by a factor of 2.

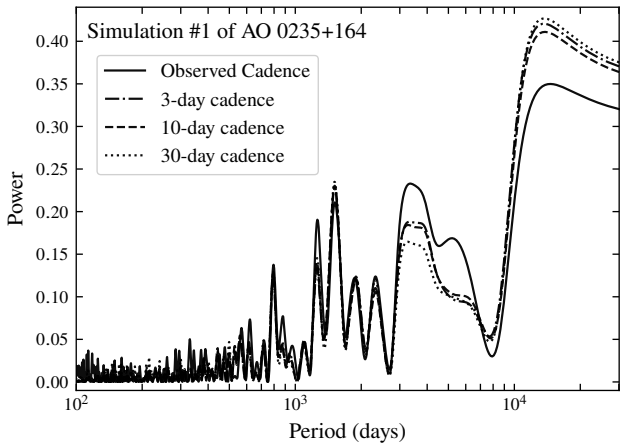

Figure 13. GLS spectra of simulations of the light curve of AO 0235+164. Since this is a simulation, we can sample it at any cadence of choice. The solid curve shows the data as actually sampled over 46 yr in the UMRAO+OVRO program. The other cadences are shown as indicated. This makes it clear that the cadence has little effect on the peak locations in the GLS spectrum, provided that the light curve is well sampled for the periods under study.

We note that this analysis does not account for nongravitational torques that are potentially expected in accreting SMBHBs (D. Lai & D. J. Muñoz 2023), in particular systems with the moderately high Eddington ratios expected for BL Lac objects (e.g., H. Dai et al. 2007). Such torques may either arrest or hasten the binary orbital decay.

Writing $N_2/N_1 = [\tau_2/\tau_1]^\alpha$, such torques can lead to $\alpha < 8/3$, but they can also lead to $\alpha > 8/3$. If dynamical forces accelerate systems to merge rapidly within a certain radius, then there should be a dearth of observable sources within that small radius, leading to $\alpha > 8/3$, but this could cause a buildup of sources around some small radius as well, leading to $\alpha < 8/3$. It depends on the scenario, but it probably will not deviate much from $\alpha = 8/3$ for SMBHBs with periods from 1–20 yr, since mergers can happen in <1 Gyr for these sources.

Given that we have detected two SMBHB candidates out of 1830 in the OVRO sample, in the combined UMRAO+OVRO sample, we expect to see strong sinusoidal variations in one out of $915 \times (16/46)^{8/3} = 55$ of the sources, i.e., we expect to see $83/55 \sim 1.5$ sources showing high-amplitude sinusoidal variations over a large fraction of their 46 yr light curves. One such source has already been found in this sample (PKS 2131–021), so there is an expectation of ∼0.43 that we will find a second such case in the combined sample, which is a reasonably high probability. Thus, although based on small numbers, which is all we have to go on in this embryonic field at this very early stage, there is a reasonable probability of detecting a second strong SMBHB candidate in the combined UMRAO+OVRO sample.

It was partly this consideration that motivated us to undertake the study of the combined UMRAO+OVRO sample—we thought that the chances of finding a second SMBHB candidate were good, which, as this paper shows, has proven to be correct.

6.2. Fractions of SMBHB Candidates in Blazar Samples

Paper II presented arguments suggesting that at least one in 100 blazars is an SMBHB candidate with orbital period in the range of months to 8 yr, where this upper limit is taken to be half the 16 yr duration of the light curves. In combining the UMRAO and OVRO light curves, this upper limit on the period has been extended to 23 yr. While the combined UMRAO+OVRO sample is not a statistically well-defined sample, it is a sample of the brightest and most rapidly flaring blazars observable from the UMRAO and OVRO, and therefore of bright rapidly flaring blazars north of decl. −20°. While PKS J1309+1154 requires confirmation as an SMBHB candidate, in our view, the combination of its power in the GLS spectrum and the hint of a harmonic in its light curve, and the consistency of the ALMA data showing almost simultaneous but slightly leading sinusoidal variations to those at 15 GHz, make it a very likely SMBHB candidate, so we will treat it as such. In this case, there are two SMBHB candidates (PKS J1309+1154 and PKS 2131–021) in our sample of 83 blazars, i.e., a fraction of 2.4%. It is useful to give a confidence interval for this fraction, which, for small numbers, can be estimated in a number of ways. The Wilson interval is $2.4^{+2.3}_{-1.2}$%, whereas assuming Poisson statistics and applying Bayes' Theorem, we find the interval to be $2.4^{+3.2}_{-0.8}$%, which we adopt for this paper.

7. Conclusion

The combined UMRAO+OVRO dataset comprising continuous monitoring of 83 blazars at frequencies 14.5/15 GHz for ∼46–50 yr is unprecedented in cadence and duration. It enables searches for periodicities of up to ∼20 yr, and

comparisons in independent long time intervals, as has been carried out here. In the analysis of the variability spectra of these 83 blazars, an in-depth search for periodicities was carried out using the GLS, WWZ, and SWF approaches. These revealed many apparent periodicities and harmonics. In order to test the significance of these periodicities and their harmonics, we generated simulated light curves with similar power-law PSD slopes to those observed in our sample. These were then analyzed using the GLS method. It was found that all but 6, 5, and 10 of the simulated GLS spectra of the simulated light curves in the $\beta = -1.5$, -1.9, and -2.5 cases, respectively (comprising 24,900 simulations in total), showed multiple periodicities and harmonics. In all three cases, we found four harmonics per source having ratios within 10% of 4/3, 3/2, 2/1, 3/1, 4/1, or their reciprocals.

The fact that multiple harmonics are seen in over ∼99.9% of the 24,900 simulations demonstrates clearly that the steep slope of the PSD combined with random flares in blazar radio light curves generate artificial periodicities and harmonics in abundance in GLS spectra.

Thus, the only case that we are aware of where this approach can be used to study the dynamics of the central engines in blazars is that where the GLS spectrum is dominated by a single GLS peak of high power. We recommend that all such studies use a power threshold of $\mathcal{P} = 0.75$ and a period allowing at least 2.5 cycles over the light-curve window.

As discussed in Paper I, a number of other studies have drawn attention to the difficulties of confirming real periodicities in blazar light curves (e.g., S. Vaughan et al. 2016; S. Covino et al. 2019; M. Tarnopolski et al. 2020; P. Peñil et al. 2025). This paper benefits, relative to other studies, from the high-cadence and ∼46 yr duration of the light curves. In addition, the statistical study of 24,900 simulated light curves makes abundantly clear the fact that great care must be taken over the interpretation of GLS variability spectra.

This study has discovered one new SMBHB candidate: PKS J1309+1154, with a radio light-curve period of 17.9 yr, but since this does not reach our 3σ threshold in the GLS spectrum, and since it has, in addition, only been observed for 2.5 cycles, we do not yet consider it to be a strong SMBHB candidate. Since the period is 17.9 yr, it will take some time to observe another cycle and confirm it as a strong candidate, but this time may be halved if the harmonic is real. In addition, optical observations might reveal evidence of shifting spectral lines that could confirm it as a strong candidate on a shorter timescale.

Apart from the fact that its X-ray spectrum is significantly harder, (i) the similarity of the morphology of PKS J1309+1154 to that of PKS 2131–021, with sinusoidal variations dominated by a bright core plus a close, stationary component that varies in concert with the core; (ii) the recently confirmed harmonic in PKS J1309+1154 (A. C. S. Readhead et al. 2026); and (iii) the small phase shift of the sinusoidal variations as a function of frequency, all support the interpretation of PKS J1309+1154 as a strong SMBHB candidate. It is clear, therefore, that PKS J1309+1154 is well worth following up across the electromagnetic spectrum.

Although the UMRAO+OVRO sample is not a carefully statistically selected sample, it is a sample of the brightest and most rapidly flaring blazars. Thus, now that PKS J1309+1154 has been confirmed as a strong SMBHB candidate (A. C. S. Readhead et al. 2026), in this cohort there are 2/83 SMBHB candidates, implying a fraction of SMBHB candidates with orbital periods up to 20 yr among bright rapidly flaring blazars of $(2.4^{+3.2}_{-0.8})\%$.

Acknowledgments

This work is supported by NSF grants AST2407603 and AST2407604. We thank the California Institute of Technology and the Max Planck Institute for Radio Astronomy for supporting the OVRO 40 m program under extremely difficult circumstances over 10 yr (2014–2024) in the absence of agency funding for operation of the telescope. Without this private support, this program would have ended in 2016. We also thank all of the volunteers who have enabled this work to be carried out. Prior to 2016, the OVRO program was supported by NASA grants NNG06GG1G, NNX08AW31G, NNX11A043G, and NNX13AQ89G from 2006–2016 and NSF grants AST-0808050 and AST-1109911 from 2008–2014. The UMRAO program received support from NSF grants AST-8021250, AST-8301234, AST-8501093, AST-8815678, AST-9120224, AST-9421979, AST-9617032, AST-9900723, AST-0307629, and AST-0607523, and earlier NSF awards, and from NASA grants NNX09AU16G, NNX10AP16G, NNX11AO13G, and NNX13AP18G. Additional funding for the operation of UMRAO was provided by the University of Michigan. W.M. acknowledges support from ANID projects Basal FB210003 and FONDECYT 11190853. A.S. and R.B acknowledge support by a grant from the Simons Foundation (00001470,RB,AS). Y.D. and F.A.H. acknowledge support through NASA under contract No. NNG08FD60C. R. R., B.M., and P.V.d.l.P. acknowledge support from ANID Basal AFB-170002, Núcleo Milenio TITANs (NCN2023_002), CATA BASAL FB210003 and UdeC-VRID 2025001479INV. T.H. acknowledges support from the Academy of Finland projects 317383, 320085, 345899, and 362571 and from the European Union ERC-2024-COG—PARTICLES—101169986. I.L. was funded by the European Union ERC-2022-STG—BOOTES—101076343. Views and opinions expressed are, however, those of the author(s) only and do not necessarily reflect those of the European Union or the European Research Council Executive Agency. Neither the European Union nor the granting authority can be held responsible for them.

This paper depended on a very large amount of VLBI data, almost all of which was taken with the Very Long Baseline Array. The National Radio Astronomy Observatory is a facility of the National Science Foundation operated under cooperative agreement by Associated Universities, Inc. This paper makes use of the following ALMA data: ADS/JAO. ALMA#2011.0.00001.CAL. ALMA is a partnership of ESO (representing its member states), NSF (USA) and NINS (Japan), together with NRC (Canada), NSTC and ASIAA (Taiwan), and KASI (Republic of Korea), in cooperation with the Republic of Chile. The Joint ALMA Observatory is operated by ESO, AUI/NRAO, and NAOJ. This research has made use of the NASA/IPAC Extragalactic Database (NED), which is funded by the National Aeronautics and Space Administration and operated by the California Institute of Technology.

Facilities: OVRO:40m, UMRAO, NRAO:VLBA, ALMA, ZTF, WISE.

Note added in proof. Since this paper was submitted, a detailed analysis has confirmed the harmonic in PKS J1309+1154 (A. C. S. Readhead et al. 2026), making this a strong SMBHB candidate.

Appendix
Sine-wave Fitting

We fitted a sine-wave model to the light curve of each of the 83 blazars using a methodology similar to that employed in Papers I, II, III, and IV. In this model, the flux density is expressed as

$$S(t) = A \sin\left(\frac{2\pi(t - t_0)}{P} - \phi_0\right) + S_0, \tag{A1}$$

where P is the sine-wave period, A is its amplitude, ϕ_0 is its phase at time $t = t_0$ (which is taken to be the mid-point of the observations for a given object), and S_0 is the mean flux density. The best-fit parameters were found by maximizing the following likelihood function:

$$\ln \mathcal{L} = -\frac{1}{2}\sum_i \left[\frac{(S_i - S(t_i))^2}{\sigma_i^2 + \sigma_0^2} + \ln(\sigma_i^2 + \sigma_0^2)\right], \tag{A2}$$

where σ_0 is a parameter that accounts for additional scatter in the light curves that is not captured by the original error bars (such as the intrinsic variability of the blazar). The posterior distributions for all model parameters were obtained using the Markov Chain Monte Carlo (MCMC) sampler by D. Foreman-Mackey et al. (2013). Note that this noise model is white noise, which does not include the effects of correlated noise, which can increase the uncertainties by a factor of up to 7. This point is discussed in detail in Appendix B of Paper II.

One significant difference compared to Papers I, II, III, and IV, is the choice of the starting points for the MCMC. For individual objects, it was possible to select the distributions of starting points by hand. However, for the entire sample of 83 blazars observed by both UMRAO and OVRO, this procedure had to be fully automated.

We used the following procedure. First, we kept the sine-wave period fixed and found the best-fit values of the parameters (A, ϕ_0, S_0, σ_0) by maximizing the likelihood function using the MCMC. We recorded the maximum value of $\ln \mathcal{L}_{\max}$ and repeated the whole procedure for a range of periods (frequencies). The starting values of A and S_0 were drawn from normal distributions with means ($\tilde{A}$, $\tilde{S}_0$) and standard deviations ($0.1\tilde{A}$, $\sigma(\tilde{S}_0)$). Here, $2\tilde{A}$ represents the difference between the 95th and 5th percentiles of the flux density, $\tilde{S}_0$ is the mean flux density, and $\sigma(\tilde{S}_0)$ is its standard deviation. The starting values of ϕ_0 and σ_0 were drawn from uniform distributions over the ranges $[0, 2\pi]$ and $[0, \sigma(\tilde{S}_0)]$, respectively.

Next, we calculated the best-fit parameters and the maximum likelihood for a range of frequencies, from $f_{\min} = 2/\Delta T$ to $f_{\max} = 1\ \mathrm{yr}^{-1}$, using a step size of $\Delta f = 0.05 f_{\min}$, where ΔT is the time span of observations. We then selected the period (frequency) with the highest likelihood value and repeated the MCMC, this time allowing the period to vary. While doing the fits, we required the period to be shorter than ΔT. We performed sine-wave fits for three datasets: combined UMRAO and OVRO, UMRAO alone, and OVRO alone. The results are reported in Table 4.

Table 4
Best-fit Periods from Sine-wave Fits

Blazar	P (days) (UMRAO)	P (days) (OVRO)	P (days) (combined)	Blazar	P (days) (UMRAO)	P (days) (OVRO)	P (days) (combined)
J0010+1058	1868 ± 8	6920^{+400}_{-316}	1845 ± 5	J1217+3007	2518^{+65}_{-56}	4843 ± 86	4401 ± 47
J0019+7327	7064^{+143}_{-136}	4666^{+61}_{-57}	4616^{+46}_{-48}	J1221+2813	16720^{+34}_{-74}	5891^{+199}_{-174}	6309 ± 66
J0050–0929	6294 ± 244	16264^{+156}_{-323}	9076 ± 225	C1224+2122	10602^{+478}_{-769}	6213^{+110}_{-102}	5922 ± 46
0059+581	1632 ± 24	2697 ± 29	1699 ± 8	J1229+0203	2987 ± 13	18192^{+169}_{-344}	3065 ± 14
J0108+0135	6686 ± 102	12039^{+2846}_{-1765}	8694 ± 116	J1256–0547	12788^{+254}_{-238}	3118^{+30}_{-28}	5220 ± 64
J0111+3906	12075^{+1772}_{-1648}	14811^{+116}_{-242}	7702^{+130}_{-123}	J1305–1033	9956^{+905}_{-1127}	2567 ± 36	2516 ± 33
J0112+2244	8995 ± 335	15455^{+726}_{-1173}	9275 ± 104	J1309+1154	6391^{+115}_{-107}	6201 ± 48	6509 ± 32
J0136+4751	12655 ± 198	1478^{+14}_{-12}	13148^{+210}_{-198}	J1310+3220	3362 ± 26	4414 ± 21	3559 ± 18
J0204+1514	16077^{+178}_{-370}	16195^{+91}_{-194}	3908 ± 27	J1337–1257	2647 ± 21	2039 ± 14	2521 ± 11
J0217+7349	4865 ± 80	2676 ± 17	2786 ± 18	J1415+1320	3206 ± 73	3670 ± 60	3262 ± 16
J0217+0144	3007 ± 27	3971 ± 40	4082 ± 27	J1419+5423	16512^{+73}_{-154}	4159 ± 47	4384 ± 22
0224+671	14456^{+810}_{-1237}	1829 ± 14	1914 ± 6	PKS1510–089	9859 ± 319	1687^{+21}_{-20}	9780 ± 197
J0237+2848	7084 ± 129	9934^{+1031}_{-734}	4942 ± 38	J1540+1447	8264^{+307}_{-263}	2997^{+40}_{-38}	8408 ± 67
J0238+1636	1988 ± 12	2501^{+36}_{-34}	2062 ± 7	J1555+1111	14314^{+567}_{-756}	10789^{+759}_{-605}	6550^{+85}_{-79}
J0259+0747	14909^{+1104}_{-1637}	11530 ± 3357	13581^{+306}_{-290}	J1613+3412	13177^{+374}_{-341}	5348 ± 44	7180 ± 36
0300+471	16416^{+378}_{-528}	15379^{+438}_{-744}	6198 ± 37	J1635+3808	9853 ± 146	967 ± 6	982 ± 3
J0309+1029	3934^{+56}_{-53}	5508^{+110}_{-98}	6860 ± 37	J1642+6856	15952^{+734}_{-1232}	16632^{+246}_{-500}	6377 ± 68
J0319+4130	17186 ± 100	18347^{+109}_{-230}	18464^{+21}_{-44}	J1642+3948	5966 ± 39	17965^{+335}_{-655}	5608 ± 48
0333+321	15686^{+460}_{-685}	15456^{+644}_{-1091}	12781 ± 156	J1653+3945	12622^{+531}_{-437}	2503 ± 33	2305 ± 11
J0339–0146	4277 ± 74	5990 ± 73	6335 ± 36	J1719+1745	2763 ± 26	7531^{+332}_{-277}	7187 ± 75
0415+379	4186^{+49}_{-53}	1539 ± 12	3784 ± 30	J1733–1304	10261^{+416}_{-355}	2866 ± 39	3767 ± 32
J0423–0120	2979 ± 22	4537 ± 35	7716 ± 85	J1740+5211	9731^{+517}_{-444}	1733 ± 13	1723 ± 5
C0424+0036	7908 ± 168	16255^{+163}_{-338}	9094 ± 71	J1743–0350	9989^{+532}_{-431}	1650 ± 8	2745 ± 13
J0433+0521	3985 ± 32	5706^{+98}_{-93}	3932 ± 21	J1748+7005	16108^{+125}_{-263}	13770^{+1676}_{-1841}	6252 ± 34
J0501–0159	13226^{+114}_{-235}	11151^{+996}_{-802}	6074 ± 87	J1751+0939	16315^{+321}_{-556}	14755^{+1404}_{-1940}	848 ± 3
J0530+1331	3761 ± 40	15895^{+150}_{-311}	3953^{+40}_{-38}	J1800+7828	13780^{+1065}_{-910}	1944^{+48}_{-43}	9821 ± 198
J0607–0834	12873^{+678}_{-572}	4794 ± 56	9242 ± 72	J1806+6949	14235^{+946}_{-831}	6612^{+139}_{-129}	6097 ± 69
J0609–1542	16442^{+131}_{-271}	2198 ± 23	4184 ± 33	J1824+5651	6840^{+201}_{-176}	3355 ± 25	3022 ± 17
J0721+7120	13095^{+646}_{-541}	12042^{+2175}_{-1680}	14777 ± 224	J1927+7358	4855^{+91}_{-84}	5133^{+130}_{-115}	7924 ± 67
PKS0727–115	6534 ± 35	17880^{+238}_{-491}	7356 ± 54	J2005+7752	11496^{+436}_{-404}	2751 ± 26	6749 ± 81
J0738+1742	11531^{+509}_{-444}	3265 ± 22	4252 ± 32	2005+403	17638^{+310}_{-486}	4263 ± 44	8768 ± 45
J0739+0137	6096 ± 119	5298^{+119}_{-110}	6536 ± 68	J2022+6136	7430^{+284}_{-256}	10956^{+1554}_{-1121}	6262 ± 95
J0757+0956	3637^{+62}_{-55}	7801^{+940}_{-629}	8138 ± 74	J2123+0535	2403 ± 15	5961^{+125}_{-117}	7184 ± 89
J0808+4950	8061^{+1980}_{-1014}	11426^{+2707}_{-1929}	4260 ± 38	PKS 2131–021	10735^{+1291}_{-639}	1787 ± 5	1723 ± 3
J0818+4222	14068^{+690}_{-580}	3800 ± 24	4632 ± 24	J2158–1501	2013 ± 33	16044^{+174}_{-365}	16246^{+24}_{-52}
J0831+0429	12916^{+980}_{-748}	14549^{+1342}_{-1796}	6501 ± 76	C2225–0457	3097 ± 16	16320^{+74}_{-158}	9066 ± 163
J0854+2006	10276 ± 100	2124 ± 25	12569^{+177}_{-167}	2230+114	12002^{+237}_{-220}	15389^{+746}_{-1354}	1464 ± 5
J0958+6533	8941^{+516}_{-422}	13226^{+275}_{-554}	6741 ± 103	J2236+2828	1087^{+3}_{-3}	6578^{+208}_{-181}	6504^{+161}_{-147}
J1058+0133	6152 ± 86	6490^{+236}_{-205}	5395 ± 62	J2253+1608	2112 ± 7	2768 ± 21	2735 ± 10
J1104+3812	16211^{+292}_{-576}	4908 ± 73	5116^{+65}_{-68}	2254+074	8179^{+649}_{-467}	3066^{+51}_{-48}	3466^{+39}_{-41}
J1150+2417	11523^{+2290}_{-1505}	13457^{+1028}_{-837}	9333 ± 94	J2348–1631	1384^{+20}_{-16}	1283 ± 9	1306 ± 6
J1159+2914	1237 ± 6	2396 ± 23	2760 ± 13	…	…	…	…

Note. PKS 2131−021 includes Haystack data from 1975–1982 (see Papers I and II).

ORCID iDs

B. Molina https://orcid.org/0009-0000-9963-6874
P. Mróz https://orcid.org/0000-0001-7016-1692
P. V. De la Parra https://orcid.org/0000-0001-5957-1412
A. C. S. Readhead https://orcid.org/0000-0001-9152-961X
T. Surti https://orcid.org/0000-0002-6369-6266
M. F. Aller https://orcid.org/0000-0003-2483-2103
J. D. Scargle https://orcid.org/0000-0001-5623-0065
R. A. Reeves https://orcid.org/0000-0001-5704-271X
H. Aller https://orcid.org/0000-0003-1945-1840
M. C. Begelman https://orcid.org/0000-0003-0936-8488
R. D. Blandford https://orcid.org/0000-0002-1854-5506
Y. Ding https://orcid.org/0000-0002-5770-2666
M. J. Graham https://orcid.org/0000-0002-3168-0139
F. Harrison https://orcid.org/0000-0002-4226-8959
T. Hovatta https://orcid.org/0000-0002-2024-8199
I. Liodakis https://orcid.org/0000-0001-9200-4006
M. L. Lister https://orcid.org/0000-0003-1315-3412
W. Max-Moerbeck https://orcid.org/0000-0002-5491-5244
V. Pavlidou https://orcid.org/0000-0002-0870-1368
T. J. Pearson https://orcid.org/0000-0001-5213-6231
V. Ravi https://orcid.org/0000-0002-7252-5485

A. G. Sullivan https://orcid.org/0000-0002-9545-7286
A. Synani https://orcid.org/0009-0004-2614-830X
K. Tassis https://orcid.org/0000-0002-8831-2038
S. E. Tremblay https://orcid.org/0000-0001-7662-2576
J. A. Zensus https://orcid.org/0000-0001-7470-3321

References

Abdollahi, S., Baldini, L., Barbiellini, G., et al. 2024, ApJ, 976, 203
Abraham, Z. 2018, NatAs, 2, 443
Agarwal, N., Agazie, G., Anumarlapudi, A., et al. 2026, ApJL, 998, L11
Agazie, G., Anumarlapudi, A., Archibald, A. M., et al. 2023, ApJL, 951, L8
Albareti, F. D., Allende Prieto, C., Almeida, A., et al. 2017, ApJS, 233, 25
Aller, H. D., Aller, M. F., Latimer, G. E., & Hodge, P. E. 1985, ApJS, 59, 513
Aller, M. F., Hughes, P. A., Aller, H. D., Latimer, G. E., & Hovatta, T. 2014, ApJ, 791, 53
An, T., Baan, W. A., Wang, J.-Y., Wang, Y., & Hong, X.-Y. 2013, MNRAS, 434, 3487
Arnaud, K. A. 1996, ASPC, 101, 17
Arshakian, T. G., Hambardzumyan, L. A., Pushkarev, A. B., & Homan, D. C. 2024, A&A, 692, A127
Arshakian, T. G., Hambardzumyan, L. A., Pushkarev, A. B., Homan, D. C., & Karapetyan, E. L. 2025, A&A, 704, A208
Arshakian, T. G., Pushkarev, A. B., Lister, M. L., & Savolainen, T. 2020, A&A, 640, A62
Baars, J. W. M., Genzel, R., Pauliny-Toth, I. I. K., & Witzel, A. 1977, A&A, 61, 99
Baluev, R. V. 2009, MNRAS, 395, 1541
Banerjee, A., Sharma, A., Mandal, A., et al. 2023, MNRAS, 523, L52
Begelman, M. C., Blandford, R. D., & Rees, M. J. 1980, Natur, 287, 307
Bellm, E. C., Kulkarni, S. R., Graham, M. J., et al. 2019, PASP, 131, 018002
Bhatta, G. 2017, ApJ, 847, 7
Blandford, R., Meier, D., & Readhead, A. 2019, ARA&A, 57, 467
Bretthorst, G. L. 2003, in Statistical Challenges in Astronomy, ed. E. D. Feigelson & G. J. Babu (Springer), 309
Britzen, S., Fendt, C., Witzel, G., et al. 2018, MNRAS, 478, 3199
Bychkova, V. S., Vol'vach, A. E., Kardashev, N. S., et al. 2015, ARep, 59, 851
Caproni, A., Mosquera Cuesta, H. J., & Abraham, Z. 2004, ApJL, 616, L99
Cohen, M. H., Meier, D. L., Arshakian, T. G., et al. 2014, ApJ, 787, 151
Cohen, M. H., Meier, D. L., Arshakian, T. G., et al. 2015, ApJ, 803, 3
Covino, S., Sandrinelli, A., & Treves, A. 2019, MNRAS, 482, 1270
Dai, H., Xie, G. Z., Zhou, S. B., et al. 2007, AJ, 133, 2187
de la Parra, P. V., Kiehlmann, S., Mróz, P., et al. 2025, ApJ, 987, 191
Dong, F.-T., Gai, N., Tang, Y., Wang, Y.-F., & Yi, T.-F. 2022, RAA, 22, 115001
Dorigo Jones, J., Johnson, S. D., Muzahid, S., et al. 2022, MNRAS, 509, 4330
Drake, A. J., Djorgovski, S. G., Mahabal, A., et al. 2009, ApJ, 696, 870
Emmanoulopoulos, D., McHardy, I. M., & Papadakis, I. E. 2013, MNRAS, 433, 907
EPTA Collaboration 2023, A&A, 678, A50
Event Horizon Telescope Collaboration, Akiyama, K., Alberdi, A., et al. 2019, ApJL, 875, L4
Foreman-Mackey, D., Hogg, D. W., Lang, D., & Goodman, J. 2013, PASP, 125, 306
Foster, G. 1996, AJ, 112, 1709
Graham, M. J., Djorgovski, S. G., Drake, A. J., et al. 2017, MNRAS, 470, 4112
Graham, M. J., Djorgovski, S. G., Stern, D., et al. 2015, Natur, 518, 74
Hincks, A. D., Ma, X., Naess, S. K., et al. 2025, arXiv:2504.04278
Johnson, S. D., Mulchaey, J. S., Chen, H.-W., et al. 2019, ApJL, 884, L31
Kelly, B. C., Becker, A. C., Sobolewska, M., Siemiginowska, A., & Uttley, P. 2014, ApJ, 788, 33
Kiehlmann, S., de la Parra, P. V., Sullivan, A. G., et al. 2025, ApJ, 985, 59
Krolik, J. H., Volonteri, M., Dubois, Y., & Devriendt, J. 2019, ApJ, 879, 110
Lai, D., & Muñoz, D. J. 2023, ARA&A, 61, 517
Li, X.-P., Yang, H.-Y., Cai, Y., et al. 2023, RAA, 23, 095010
Liao, G., Chen, X., Zheng, Q., Liu, Y., & Zhang, X. 2025, A&A, 698, A265
Lister, M. L., Homan, D. C., Kellermann, K. I., et al. 2021, ApJ, 923, 30
Lister, M. L., Homan, D. C., Kellermann, K. I., et al. 2023, MOJAVE. XVIII. Bright radio-loud active AGNs, CDS/VizieR Catalogue, doi:10.26093/cds/vizier.19230030
Liu, F. K., Zhao, G., & Wu, X.-B. 2006, ApJ, 650, 749
Lomb, N. R. 1976, Ap&SS, 39, 447
Mainzer, A., Bauer, J., Grav, T., et al. 2011, ApJ, 731, 53
Mao, L., & Zhang, X. 2024, MNRAS, 531, 3927
Miles, M. T., Shannon, R. M., Bailes, M., et al. 2023, MNRAS, 519, 3976
O'Neill, S., Kiehlmann, S., Readhead, A. C. S., et al. 2022, ApJL, 926, L35
Peñil, P., Domínguez, A., Buson, S., et al. 2025, MNRAS, 543, 2880
Pearson, T. J., & Readhead, A. C. S. 1984, ARA&A, 22, 97
Pushkarev, A. B., Aller, H. D., Aller, M. F., et al. 2023, MNRAS, 520, 6053
Ragazzini, J. R., & Zadeh, L. A. 1952, TAIEE, 71, 225
Readhead, A. C. S., Aller, M. F., Sullivan, A. G., et al. 2026, ApJL, 996, L39
Readhead, A. C. S., Lawrence, C. R., Myers, S. T., et al. 1989, ApJ, 346, 566
Ren, G.-W., Ding, N., Zhang, X., et al. 2021a, MNRAS, 506, 3791
Ren, G.-W., Zhang, H.-J., Zhang, X., et al. 2021b, RAA, 21, 075
Richards, G. T., Myers, A. D., Gray, A. G., et al. 2009, ApJS, 180, 67
Richards, J. L., Max-Moerbeck, W., Pavlidou, V., et al. 2011, ApJS, 194, 29
Roy, M., Papadakis, I. E., Ramos-Colón, E., et al. 2000, ApJ, 545, 758
Scargle, J. D. 1982, ApJ, 263, 835
Seilmayer, M., Garcia Gonzalez, F., & Wondrak, T. 2020, arXiv:2001.10200
Sharma, A., Prince, R., & Bose, D. 2023, arXiv:2312.12623
Shepherd, M. C. 1997, ASPC, 125, 77
Shepherd, M. C., Pearson, T. J., & Taylor, G. B. 1994, BAAS, 26, 987
Sullivan, A. G., Blandford, R. D., Synani, A., et al. 2026, ApJ, 997, 85
Tang, Y., Haiman, Z., & MacFadyen, A. 2018, MNRAS, 476, 2249
Tarnopolski, M., Żywucka, N., Marchenko, V., & Pascual-Granado, J. 2020, ApJS, 250, 1
Timmer, J., & Koenig, M. 1995, A&A, 300, 707
Tripathi, A., Gupta, A. C., Aller, M. F., et al. 2021, MNRAS, 501, 5997
VanderPlas, J. T., & Ivezić, Ž. 2015, ApJ, 812, 18
Vaughan, S., Uttley, P., Markowitz, A. G., et al. 2016, MNRAS, 461, 3145
Wang, J.-Y., An, T., Baan, W. A., & Lu, X.-L. 2014, MNRAS, 443, 58
Wang, J.-y., Lu, X.-l., Zhao, Q.-w., et al. 2017, ChA&A, 41, 42
Weaver, Z. R., Jorstad, S. G., Marscher, A. P., et al. 2022, ApJS, 260, 12
Wright, E. L., Eisenhardt, P. R. M., Mainzer, A. K., et al. 2019, NASA IPAC DataSet, IRSA1, doi:10.26131/IRSA1
Zechmeister, M., & Kürster, M. 2009, A&A, 496, 577